

Microstructure and magnetic properties of FeCoZr(Mo)BGe nanocrystalline alloys

Wanqiu Yu(于万秋), Yanxiang Sun(孙筵翔), Lihua Liu(刘立华), and Pingli Zhang(张平丽)
Citation: Chin. Phys. B, 2025, 34 (**1**): 016102. DOI: 10.1088/1674-1056/ad5a77

What follows is a list of articles you may be interested in

Correlation of microstructure and magnetic softness of Si-microalloying FeNiBCuSi nanocrystalline alloy revealed by nanoindentation

Benjun Wang(汪本军), Wenjun Liu(刘文君), Li Liu(刘莉), Yu Wang(王玉), Yu Hang(杭宇), Xinyu Wang(王新宇), Mengen Shi(施蒙恩), Hanchen Feng(冯汉臣), Long Hou(侯龙), Chenchen Yuan(袁晨晨), Zhong Li(李忠), and Weihuo Li(李维火)
Chin. Phys. B, 2024, 33 (**12**): 126101. DOI: 10.1088/1674-1056/ad84c8

Liquid crystal droplets formation and stabilization during phase transition process

Xia Meng(孟霞), Jiayao Ye(叶家耀), Ao Li(李澳), Xudong Zhu(朱徐栋), Zhaoyan Yang(杨朝雁), Lei Wang(王磊), Bingxiang Li(李炳祥), and Yanqing Lu(陆延青)
Chin. Phys. B, 2024, 33 (**11**): 116101. DOI: 10.1088/1674-1056/ad7afd

Pressure-induced structural, electronic, and superconducting phase transitions in $TaSe_3$

Yuhang Li(李宇航), Pei Zhou(周佩), Chi Ding(丁驰), Qing Lu(鲁清), Xiaomeng Wang(王晓梦), and Jian Sun(孙建)
Chin. Phys. B, 2024, 33 (**10**): 106102. DOI: 10.1088/1674-1056/ad6f92

Visualizing extended defects at the atomic level in a $Bi_2Sr_2CaCu_2O_{8+\delta}$ superconducting wire

Kejun Hu(胡柯钧), Shuai Wang(王帅), Boyu Li(李泊玉), Ying Liu(刘影), Binghui Ge(葛炳辉), and Dongsheng Song(宋东升)
Chin. Phys. B, 2024, 33 (**9**): 096101. DOI: 10.1088/1674-1056/ad6ccd

Electronic effects on radiation damage in α-iron: A molecular dynamics study

Lin Jiang(江林), Min Li(李敏), Bao-Qin Fu(付宝勤), Jie-Chao Cui(崔节超), and Qing Hou(侯氢)
Chin. Phys. B, 2024, 33 (**3**): 036103. DOI: 10.1088/1674-1056/ad0ec4

Microstructure and magnetic properties of FeCoZr(Mo)BGe nanocrystalline alloys

Wanqiu Yu(于万秋)[1,†], Yanxiang Sun(孙筵翔)[2], Lihua Liu(刘立华)[1], and Pingli Zhang(张平丽)[1]

[1] *College of Physics, Jilin Normal University, Siping* 136000, *China*
[2] *Chengxi Power Supply Company, State Grid Tianjin Electric Power Company, Tianjin* 300190, *China*

(Received 23 April 2024; revised manuscript received 13 June 2024; accepted manuscript online 21 June 2024)

The microstructure and magnetic properties of $Fe_{40}Co_{40}Zr_9B_{10}Ge_1$ (Mo-free) and $Fe_{40}Co_{40}Zr_5Mo_4B_{10}Ge_1$ (Mo-containing) nanocrystalline alloys, prepared using an amorphous crystallization method, were investigated. Mo addition affects the crystallization of the $Fe_{40}Co_{40}Zr_9B_{10}Ge_1$ amorphous alloy and decreases the grain size of the α-Fe(Co) phase below 650 °C. For the Mo-free alloy annealed at 600 °C and the Mo-containing alloy annealed at 575 °C, with a single α-Fe(Co) crystallization phase and approximately similar crystallization volume fractions, the Mo-containing alloy showed smaller, more regularly shaped grains and a significantly narrower grain-size distribution than the Mo-free alloy. The Fe and Co contents in the nanograins of the two alloys also differed. For the Mo-free alloy, a higher concentration of Co distributed in the residual amorphous matrix. For the Mo-containing alloy, a higher concentration Co dissolved in the nanograins. The specific saturation magnetization and coercivity of the Mo-free alloy were 1.05- and 1.59-times higher than those of the Mo-containing alloy, respectively.

Keywords: nanostructured materials, Mo addition, microstructure, grain size

PACS: 61.43.Dq, 61.46.Hk, 75.75.–c, 81.07.–b

DOI: 10.1088/1674-1056/ad5a77 **CSTR:** 32038.14.CPB.ad5a77

1. Introduction

Fe-based soft magnetic alloys with a dual-phase nanocrystalline–amorphous structure are often prepared using a rapid solidification (melt spinning) method to achieve the amorphous phase, followed by controlled heat treatment. Excellent soft magnetism is realized when fine ferromagnetic nanocrystallites are exchange-coupled with a surrounding amorphous matrix. (Fe, Co)-based soft magnetic alloys have been extensively studied for use as a viable alternative to Si steels. Considerable efforts have been devoted to improving their magnetic properties to achieve high saturation magnetic induction (B_s) and low core loss, thereby increasing the efficiency of electrical machines and saving energy.[1] (Fe, Co)-based soft magnetic alloys are important Fe-based nanocrystalline soft magnetic materials, and they have gained considerable attention because of their excellent soft magnetic properties. These alloys are prepared by partially substituting Fe with Co, resulting in high saturation magnetization and Curie temperatures (T_c).[2] Our research group has extensively investigated an FeCo-based soft magnetic alloy system.[3–8] The crystallization of FeCoZrB system alloys,[4,5] as well as the effect of heat treatment[3] and the addition of different elements[6–8] on the microstructure and magnetic properties of FeCoZrB alloys, have been examined. The magnetic properties of nanocrystalline ribbons are significantly affected by structural and compositional variations.[9] The doping of FeCo-based alloys significantly affects the structure and performance of the adjusted microstructures and improves the properties of FeCo-based alloys.[10–18] Understanding the effect of element doping on microstructural features and soft magnetic behavior is crucial.[19]

For Fe-based nanocrystalline soft magnetic alloys, Cu-rich clusters are considered the key factor in achieving smaller grain sizes.[20–24] To extend the flexibility of applications for Fe-based nanocrystalline alloys, elements other than Cu that promote nanocrystalline formation must be assessed. However, for Zr-containing HITPERM [Fe(Co)–*M*–B–Cu (*M* = Nb, Zr, Hf, etc.)]-type alloys with an α-(Fe, Co) crystallizing phase, there is no significant difference in grain size between samples with and without Cu.[25] For Zr-containing HITPERM-type alloys, additional elements (other than Cu) must be identified to reduce the grain size. The effects of Nb and Mo contents on the microstructures and properties of an $Fe_{40}Co_{40}Zr_9B_{10}Ge_1$ alloy were investigated and compared.[26] With increasing Nb or Mo content (1 at.%–4 at.%), the primary crystallization temperature, grain size of the α-Fe(Co) phase, and coercivity decreased. Moreover, the thermal behavior, grain size, and coercivity of the alloys were more significantly affected by the addition of Mo than that of Nb. For the $Fe_{40}Co_{40}Zr_9B_{10}Ge_1$ alloy, the addition of 4-at.% Mo yielded the best results. Introducing 4-at.% Mo as a nanocrystalline-forming element serves as an effective approach for designing FeCoZrB alloy systems. However, the

†Corresponding author. E-mail: yuwanqiu2004@126.com

© 2025 Chinese Physical Society and IOP Publishing Ltd. All rights, including for text and data mining, AI training, and similar technologies, are reserved.

crystallization, elemental distribution, and magnetization of the $Fe_{40}Co_{40}Zr_5Mo_4B_{10}Ge_1$ alloy require further investigation.

To this end, in this study, $Fe_{40}Co_{40}Zr_9B_{10}Ge_1$ (Mo-free) and $Fe_{40}Co_{40}Zr_5Mo_4B_{10}Ge_1$ (Mo-containing) alloys were prepared, and their microstructure and magnetic properties were examined. The change in elemental distribution induced by Mo addition was studied through scanning transmission electron microscopy–energy dispersive spectroscopy (STEM–EDS). The microstructure, elemental distribution, and magnetic properties of the two types of alloys were studied and compared.

2. Materials and methods

Ingots with nominal compositions of $Fe_{40}Co_{40}Zr_9B_{10}Ge_1$ and $Fe_{40}Co_{40}Zr_5Mo_4B_{10}Ge_1$ were prepared by arc melting mixtures of pure elements (99.98-wt% Fe, 99.99-wt% Co, 99.92-wt% Zr, 99.95-wt% Mo, 99.99-wt% B, 99.99-wt% Ge). The mixtures were remelted four times with magnetic stirring in a pure argon atmosphere to ensure homogeneity. The corresponding amorphous ribbons of approximately 30-μm thickness and 1-cm width were prepared via single-roller melt spinning (with a copper-wheel rate of 38 m/s) and isothermal annealing in a vacuum. Differential scanning calorimetry (DSC) of the amorphous alloys was conducted using a simultaneous thermal analyzer (STA, 449F5). According to the DSC curves, the as-quenched Mo-free alloy was annealed at 540 °C, 575 °C, 600 °C, 650 °C, 675 °C, and 725 °C, and the as-quenched Mo-containing alloy was annealed at 480 °C, 540 °C, 575 °C, 615 °C, 650 °C, and 715 °C. The structural characterization of the alloys was performed using x-ray diffractometry (XRD, Rigaku D/max 2500/PC, Cu-$K\alpha$, $\lambda = 1.5406$ Å, 40 kV, 200 mA, scan speed: 4 °/min) and transmission electron microscopy (TEM, FEI Talos F200). The grain size of α-Fe(Co) was calculated using Jade 5.0. STEM–EDS was performed to determine the elemental concentration. Digital Micrograph (Version 3.5.2, Gatan) was used to analyze the TEM images. The grain-size distributions were obtained using the Nano Measurer tool (version 1.2). Hysteresis loops were measured using a physical property measurement system (PPMS, Dynacool-9T) to obtain the specific saturation magnetization (M_s). The coercivity (H_c) was obtained using a DC *B–H* loop tracer (Riken Denshi BHS40).

3. Results and discussion

The DSC curves of the $Fe_{40}Co_{40}Zr_9B_{10}Ge_1$ (Mo-free) and $Fe_{40}Co_{40}Zr_5Mo_4B_{10}Ge_1$ (Mo-containing) alloys are shown in the following Fig. 1. The Mo-free alloy exhibits three exothermic peaks and three stages of crystallization. The addition of the 4-at.% Mo reduces the primary crystallization temperature. Two exothermic peaks are subsequently observed in the DSC plot of the Mo-containing alloy, indicating a two-stage crystallization process.

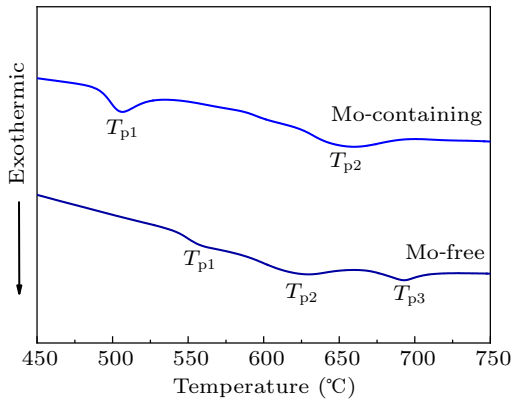


Fig. 1. DSC curves of the Mo-free and Mo-containing alloys as-quenched.

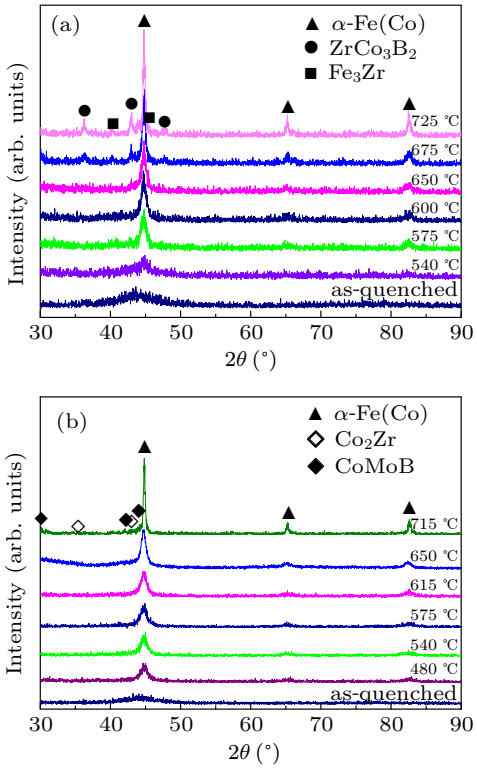


Fig. 2. XRD patterns of the (a) Mo-free and (b) Mo-containing alloys as-quenched and after annealing.

Furthermore, the XRD patterns of the as-quenched Mo-free and Mo-containing alloys, and those annealed at different temperatures, are shown in Fig. 2. The XRD patterns of the two types of as-quenched alloys exhibit a unique broad and diffuse amorphous peak, indicating that they are amorphous in the quenched state. Compared with the as-quenched alloy, the XRD pattern of the Mo-free alloy annealed at 540 °C did not significantly change. At 575 °C and 600 °C, the α-Fe(Co) phase can be clearly seen. When the temperature is above 650 °C, $ZrCo_3B_2$ and Fe_3Zr phases form in addition to an α-Fe(Co) phase. For the Mo-containing alloy, only the α-Fe(Co) phase precipitates from the amorphous matrix at 480 °C, and

the volume crystallization fraction increases with the annealing temperature. At 715 °C, Co_2Zr and CoMoB phases form in addition to the α-Fe(Co) phase.

Figure 3 shows the grain size of the α-Fe(Co) phase as a function of annealing temperature (T_a). Below 650 °C, the grain size of the α-Fe(Co) phase of the Mo-containing alloy is smaller than that of the Mo-free alloy.

Figure 4 shows the high-resolution transmission electron microscopy (HRTEM) and corresponding fast Fourier transform (FFT) images of the Mo-free alloy annealed at 540 °C. Using Digital Micrograph, the distance and angle between each diffraction spot and the center spot were measured to determine the crystal structure and obtain the crystal plane index corresponding to the diffraction spot. Thus, we determined the small grain to be a β-Mn type phase grain with a crystal band axis of [411]. The metastable β-Mn type phase was also observed in other Fe-based alloys.[27,28]

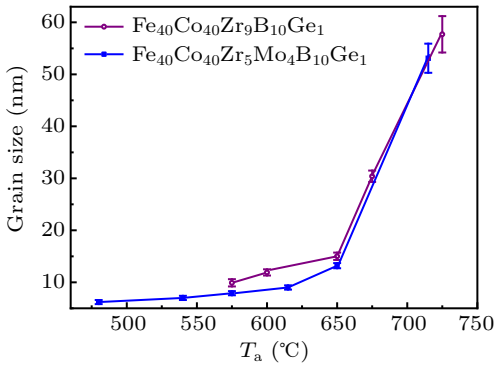


Fig. 3. Grain size of the α-Fe(Co) phase as a function of annealing temperature (T_a).

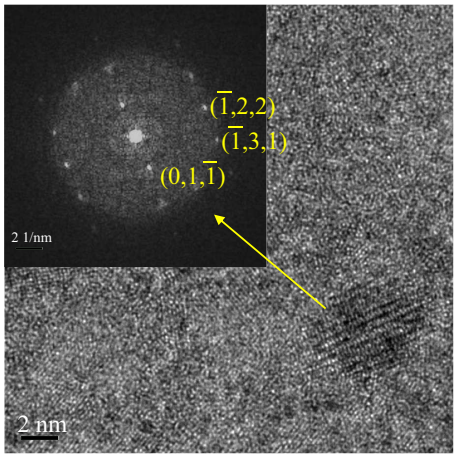


Fig. 4. HRTEM and FFT images of the Mo-free alloy annealed at 540 °C.

From the before mentioned analysis, it can be inferred that the three exothermic peaks in the DSC curve of the Mo-free amorphous alloy correspond to the formation of the α-Fe(Co) and β-Mn-type phases, the growth of an α-Fe(Co) volume fraction at the expense of the β-Mn and residual amorphous phases, and the precipitation of $ZrCo_3B_2$ and Fe_3Zr intermetallic compounds. The two exothermic peaks in the DSC curve of the Mo-containing amorphous alloy correspond to the formation of α-Fe(Co), the growth of the α-Fe(Co) volume fraction at the expense of the residual amorphous phase and the precipitation of CoMoB and Co_2Zr intermetallic compounds.

Figure 5 shows the XRD patterns of the Mo-free alloy annealed at 600 °C (a) and the Mo-containing alloy annealed at 575 °C (b). Both crystallization phases were a single α-Fe(Co) phase with approximately similar crystallization volume fractions. Therefore, the Mo-free alloy annealed at 600 °C and the Mo-containing alloy annealed at 575 °C were selected for further experiments. Their microstructure, elemental distribution, and magnetic properties of the two kinds of alloys with approximately similar crystallization volume fractions are studied and compared.

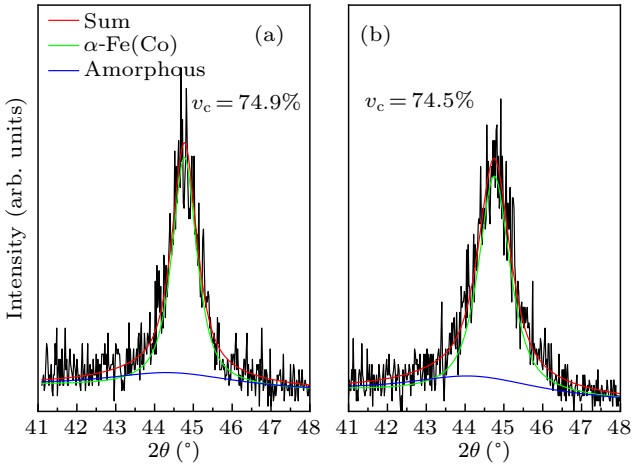


Fig. 5. XRD patterns of the Mo-free alloy annealed at (a) 600 °C and (b) the Mo-containing alloy annealed at 575 °C.

Figure 6 shows the TEM images and corresponding selected-area electron diffraction (SAED) patterns, as well as the HRTEM images and corresponding FFT patterns of the Mo-free alloy annealed at 600 °C and the Mo-containing alloy annealed at 575 °C. The SAED patterns only display the α-Fe(Co) phase, and the TEM images illustrate the α-Fe(Co) nanocrystals distributed in the residual amorphous phase of the two alloys. Some grain aggregation occurs in the Mo-free alloy. For the Mo-containing alloy, the grains are uniformly distributed, the grain size is small, and the shape is uniform. The α-Fe(Co) nanocrystal is uniformly embedded in the remaining amorphous matrix. The grain distribution of Mo-containing alloys is more uniform than that of Mo-free alloy. The FFT images indicate that both grains possess the α-Fe(Co) phase. In both HRTEM images, no other crystalline phases are observed. Two hundred spots were collected from the TEM images (Figs. 6(a) and 6(b)); the grain-size distributions are shown in Figs. 6(a3) and 6(b3). The grain-size distributions were fitted using a log-normal function.[29]

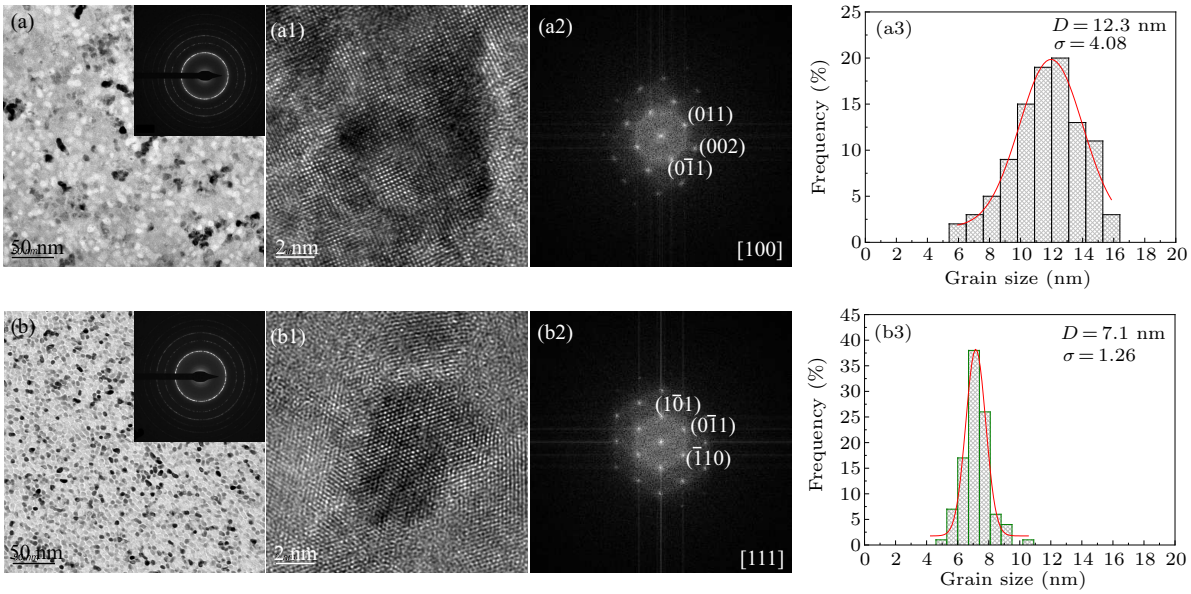


Fig. 6. TEM images, SAED patterns, HRTEM images, FFT patterns, and grain-size distributions of [panels (a), (a1), (a2), (a3)] the Mo-free alloy annealed at 600 °C, and [panels (b), (b1), (b2), (b3)] the Mo-containing alloy annealed at 575 °C, respectively.

Based on the fitting results, the mean grain size of the Mo-free alloy is 12.3 nm, and that of the Mo-containing alloy is 7.1 nm. The width of the grain-size distribution can be determined by the geometric standard deviation (σ).[30] The σ value of the Mo-containing alloy is significantly less than that of the Mo-free alloy. The uniformity of grain-size distribution of Mo-containing alloys is higher than that of FeCo-based alloys reported in the literature.[31–37]

The partitioning behavior of the alloying elements was evaluated through EDS line-scan analysis. The EDS line scans for the Mo-free alloy annealed at 600 °C and the Mo-containing alloy annealed at 575 °C are shown in Fig. 7. For the Mo-free alloy, grain aggregation was clearly observed. The EDS results correspond to the straight line in the TEM images. The remaining amorphous matrix was rich in Zr. The nanocrystals contained Fe and Co, with the content of Fe being higher than that of Co. The Co content of the remaining amorphous phase was higher than that of the nanocrystals. This finding is consistent with the results reported by Ping *et al.*,[25] who found that for the $Fe_{44}Co_{44}Zr_7B_4Cu_1$ alloy, Co was preferentially partitioned in the remaining amorphous phase. For the Mo-containing alloy, the remaining amorphous matrix was rich in both Zr and Mo. The grains contained Fe and Co, and the Fe and Co contents of the nanocrystals or remaining amorphous matrix were similar. Furthermore, the Fe and Co contents of the remaining amorphous phase were lower than those of the nanocrystals.

The Fe and Co contents in the grains of the Mo-free and Mo-containing alloys differed significantly. For the Mo-free alloy, Co was preferentially partitioned into the remaining amorphous phase owing to the strong pair interaction between Co and Zr. However, for the Mo-containing alloy, Co was preferentially partitioned in the nanocrystals owing to the 4-at.% Mo substitution of Zr.

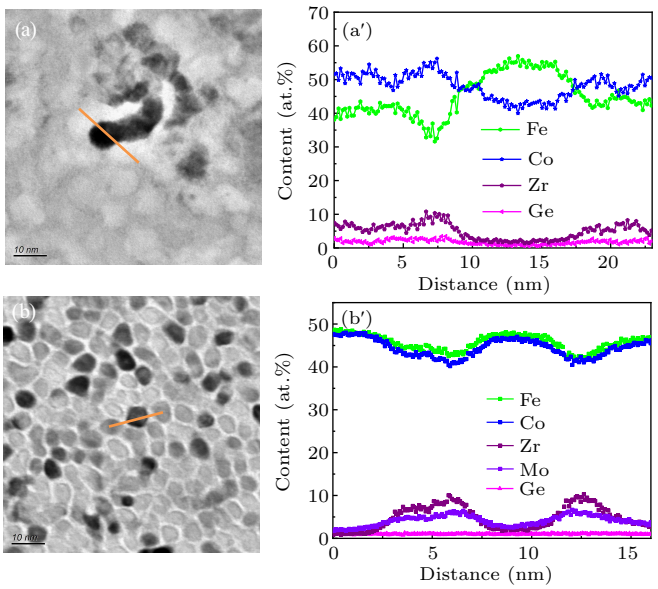


Fig. 7. (a), (b) TEM images and (a′), (b′) STEM–EDS line scans of the [(a), (a′)] Mo-free alloy annealed at 600 °C and [(b), (b′)] Mo-containing alloy annealed at 575 °C.

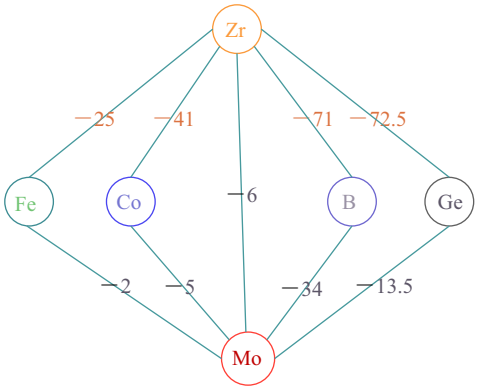


Fig. 8. Enthalpy of mixing (in units of kJ/mol) between Zr/Mo and other elements.

Figure 8 shows the enthalpy of mixing Zr/Mo with other elements.[38] Compared to Zr, Mo had a smaller negative enthalpy when mixed with other elements.

Zr and Mo underwent slow diffusion in the amorphous matrix and exhibited low solid solubility in α-Fe(Co), inhibiting grain growth during initial crystallization. For the Mo-free alloy, because of the large negative mixing heat among Zr, Co, and B, a $ZrCo_3B_2$ phase was easily formed at high annealing temperatures, as confirmed by the XRD pattern of the Mo-free alloy above 650 °C (Fig. 2(a)). Zr distributed in the remaining amorphous phase can inhibit grain growth. The precipitation of the $ZrCo_3B_2$ phase decreased the Zr content of the amorphous matrix, resulting in a faster increase in grain size at high temperatures. For the Mo-containing alloy, a rapid increase in grain size at high annealing temperatures was observed owing to the precipitation of compounds containing Zr and Mo.

For Zr-containing HITPERM-type alloys, the addition of Mo is instrumental in refining grain size, similar to the effect of Cu in other Fe-based alloys. The difference is that for Cu-containing Fe-based alloys, the Cu clusters serve as heterogeneous nucleation sites for the initial α-Fe particles.[22]

As shown in Fig. 9, the specific M_s value (163.8 emu/g) of the Mo-free alloy annealed at 600 °C was slightly higher than that of the Mo-containing alloy (155.7 emu/g) annealed at 575 °C. The H_c of the Mo-containing alloy (62.8 A/m) was lower than that of the Mo-free alloy (100.2 A/m). Furthermore, M_s of the Mo-free alloy was 1.05 times higher than that of the Mo-containing alloy, and H_c was 1.59-times higher than that of the Mo-containing alloy.

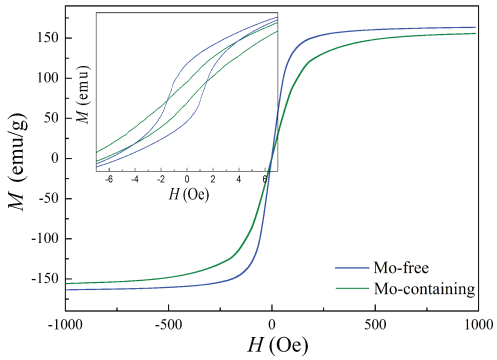


Fig. 9. Hysteresis loops of the Mo-free alloy annealed at 600 °C and the Mo-containing alloy annealed at 575 °C. The unit 1 Oe = 79.5775 A·m^{-1}.

According to the Slater–Pauling curve,[39,40] the highest saturation magnetization occurred in the $Fe_{65}Co_{35}$ alloy. Müller *et al.*[41] found that in the FeCoZrBCu system, a maximum B_s of 1.67 T was obtained at about 35-at.% Co. Subsequently, as the Co content of the alloy increased above 35 at.%, the magnetic moment decreased. Furthermore, the M_s also depends on the crystalline volume fraction through the proportion of the different phases contributing to the total magnetization of the sample,[42] as expressed below:

$$M_s = M_{Am}(1-x) + M_{Cr}(x),$$

where M_{Am} and M_{Cr} are the saturation magnetization of the amorphous and crystalline phases, respectively. In this study, the Mo-free alloy annealed at 600 °C and the Mo-containing alloy annealed at 575 °C have similar crystallization volume fractions.

The proportion of Co in the Fe(Co) nanograins was approximately 44% for the Mo-containing alloy and approximately 53% for the Mo-free alloy (according to Fig. 7). The saturation magnetization of the crystalline phase of the Mo-free alloy was higher than that of the 4-at.% Mo-containing alloy. The magnetization of M_{Am} is known to be lower than that of M_{Cr}. Thus, the saturation magnetization of the alloy was determined by M_{Cr}. Furthermore, the crystallization volume fraction of the crystalline phase was larger than that of the amorphous phase. Therefore, the saturation magnetization of the Mo-free alloy was slightly higher than that of the 4-at.% Mo-containing alloy. For the nanocrystalline–amorphous two-phase alloy, based on the random anisotropy model,[43,44] the intergranular magnetic coupling between adjacent nanocrystals through the residual amorphous phase suppresses the magnetocrystalline anisotropy in the range $D < L_{ex}$, where L_{ex} is the exchange–correlation length. Bitoh *et al.*[30] suggested that the log-normal distribution function can be expressed as follows: $\langle K\rangle \approx K_1^4\langle D\rangle^6 \exp(6\sigma_D^2)/(\varphi^6 A_c^3)$, where K_1 is the magnetocrystalline anisotropy constant, φ is the parameter that reflects the symmetry of $\langle K_1\rangle$ as well as the total spin rotation angle over the exchange-correlated coupling chain, A_c is the exchange stiffness constant, $\langle D\rangle$ is the mean grain size, and σ_D is the geometric standard deviation of the distribution. The mean grain size of the Mo-free alloy is larger than that of the Mo-containing alloy. The σ value for the Mo-containing alloy is significantly less than that for the Mo-free alloy. Furthermore, the grains of the Mo-containing alloy are distributed more uniformly. Therefore, the H_c of the Mo-containing alloy is lower than that of the Mo-free alloy.

4. Conclusion and perspectives

(i) Mo addition affects the crystallization of the $Fe_{40}Co_{40}Zr_9B_{10}Ge_1$ amorphous alloy. There are three stages in the crystallization of the $Fe_{40}Co_{40}Zr_9B_{10}Ge_1$ (Mo-free) amorphous alloy, and there are two stages in the crystallization of the $Fe_{40}Co_{40}Zr_5Mo_4B_{10}Ge_1$ (Mo-containing) amorphous alloy.

(ii) Below 650 °C, the grain size of the α-Fe(Co) phase of the Mo-containing alloy is smaller than that of the Mo-free alloy.

(iii) Both the Mo-free alloy annealed at 600 °C and the Mo-containing alloy annealed at 575 °C have a single α-Fe(Co) crystallization phase with approximately similar crystallization volume fractions.

(iv) Grain aggregation was observed in the Mo-free alloy. Small and uniformly distributed grains with uniform shapes were observed in the Mo-containing alloy. The geometric standard deviation of the Mo-containing alloy was significantly lower than that of the Mo-free alloy.

(v) The Fe and Co contents in the nanograins of the Mo-free and Mo-containing alloys significantly differed. For the Mo-free alloy, the Fe content in the nanocrystals was higher than the Co content. The Co content in the remaining amorphous phase was higher than that of the nanocrystals. For the Mo-containing alloy, the Fe and Co contents of the nanocrystals were similar. The Fe and Co contents of the remaining amorphous phase were lower than those of the nanocrystals.

(vi) The specific saturation magnetization and coercivity of the Mo-free alloy were 1.05- and 1.59-times higher than those of the Mo-containing alloy, respectively.

(vii) The conclusions [(iv)–(vi)] are based on the comparison of two alloys with similar crystallization volume fractions in the experiment; other experimental research and theoretical investigation are needed to supplement the effect of Mo substitution in the future.

Acknowledgements

Project supported by the Natural Science Foundation of Jilin Province, China (Grant No. YDZJ202201ZYTS319) and the Fund from Sinoma Institute of Materials Research (Guangzhou) Co., Ltd. (SIMR) for assisting with the TEM characterization. We would like to thank Editage (www.editage.cn) for English language editing.

References

[1] Jafari S, Beitollahi A, Eftekhari Yekta B, Ohkubo T, Budinsky V, Marsilius M, Mollazadeh S, Herzer G and Hono K 2016 *J. Magn. Magn. Mater.* **401** 1123
[2] Willard M A, Laughlin D E, Mchenry M E, Thoma D, Sickafus K, Cross J O and Harris V G 1998 *J. Appl. Phys.* **84** 6773
[3] Yu W Q, Zeng H Q, Sun Y M, Sun Y J and Hua Z 2017 *Phys. Lett. A* **381** 1573
[4] Yu W Q, Sun Y M and Hua Z 2011 *Appl. Surf. Sci.* **257** 9733
[5] Yu W Q, Lu L P, Zuo B, Hua Z, Xing G L, Wang X Y and Wang D D 2019 *Appl. Phys. A* **125** 636
[6] Yu W Q, Zeng H Q, Sun Y M and Hua Z 2017 *Vacuum* **137** 175
[7] Yu W Q, Tian B, Wang Z Q, Liu Y D and Sun Y M 2022 *Rare Met. Mater. Eng.* **51** 1735
[8] Yu W Q, Sun Y M, Liu Y D, Liu J, Zuo B, Liu L H, Dong L R and Hua Z 2012 *Optoelectron. Adv. Mater. Rapid Commun.* **6** 145
[9] Lian L Y, Zhang X W, Liu Y, Li J and Wang R Q 2023 *Chin. Phys. B* **32** 077501
[10] Hao Q Q, Wang Z, Li X H, Zhang Y and Shi R M 2021 *Physica B* **604** 412701
[11] Zhang L, Wang Z and Xu Y C 2018 *J. Non-Cryst. Solids* **481** 148
[12] Sun Y and Bi X 2011 *J. Alloys Compd.* **509** 1665
[13] Blázquez J S, Franco V, Conde A and Kiss L F 2003 *J. Magn. Magn. Mater.* **262** 170
[14] Li Y, Wang Z and Zhang W 2018 *AIP Adv.* **8** 056115
[15] Nabiałek M, Jeż B and Błoch K 2020 *Metall. Mater. Trans. A* **51** 4602
[16] Kucuk I, Aykol M, Uzun O, Yildirim M, Kabaer M, Duman N, Yilmaz F, Erturk K, Akdeniz M V and Mekhrabov A O 2011 *J. Alloys Compd.* **509** 2334
[17] Alleg S, Souilah S, Younes A, Bensalem R, Suñol J J and Greneche J M 2012 *J. Alloys Compd.* **536** S394
[18] Li X H, Wang Z and Duan H J 2019 *J. Non-Cryst. Solids* **517** 114
[19] Lashgari H R, Chu D, Xie S, Sun H, Ferry M and Li S 2014 *J. Non-Cryst. Solids* **391** 61
[20] Akase Z, Kimura K, Saito T, Niitsu K, Tanigaki T, Iwasaki Y, Sharma P, Makino A and Shindo D 2022 *J. Magn. Magn. Mater.* **541** 168519
[21] Xu J, Liu X, Wang G, Luo T, Wang J, Lu K and Yang Y 2021 *J. Alloys Compd.* **859** 157850
[22] Hono K, Ping D H, Ohnuma M and Onodera H 1999 *Acta Mater.* **47** 997
[23] Ohkubo T, Kai H, Ping D H, Hono K and Hirotsu Y 2001 *Scr. Mater.* **44** 971
[24] Jha R, Diercks D R, Chakraborti N, Stebner A P and Ciobanu C V 2019 *Scr. Mater.* **162** 331
[25] Ping D H, Wu Y Q, Hono K, Willard M A, Mchenry M E and Laughlin D E 2001 *Scr. Mater.* **45** 781
[26] Sun Y M, Wang Z Q, Xu S C and Hua Z 2021 *Chin. Phys. B* **30** 038103
[27] Lyasotsky I V, Dyakonova N B and Dyakonov D L 2014 *J. Alloys Compd.* **586** S20
[28] Dyakonova N B, Dyakonov D L and Lyasotskyi I V 2014 *J. Alloys Compd.* **586** S41
[29] Pradeep K G, Herzer G, Choi P and Raabe D 2014 *Acta Mater.* **68** 295
[30] Bitoh T, Makino A, Inoue A and Masumoto T 2003 *Mater. Trans.* **44** 2011
[31] Prabhu D, Veerababu R, Balamuralikrishnan R, Narayanasamy A and Chattopadhyay K 2012 *Mater. Sci. Eng. B* **177** 791
[32] Xue L, Yang W M, Liu H S, Men H, Wang A D, Chang C T and Shen B L 2016 *J. Magn. Magn. Mater.* **419** 198
[33] Miao B, Luo Q, Chang C, Liu T, Zhang Y and Shen J 2019 *J. Magn. Magn. Mater.* **477** 156
[34] Roy R K, Panda A K and Mitra A 2016 *J. Magn. Magn. Mater.* **418** 236
[35] Hou L, Fan X, Wang Q, Yang W and Shen B 2019 *J. Mater. Sci. Technol.* **35** 1655
[36] Hawelek L, Polak M, Wlodarczyk P, Zackiewicz P, Radon A, Lukowiec D, Hreczka M and Kolano-Burian A 2020 *J. Magn. Magn. Mater.* **512** 166681
[37] Kunca B, Marcin J, Švec P sr and Škorvánek I 2024 *J. Magn. Magn. Mater.* **591** 171679
[38] Takeuchi A and Inoue A 2005 *Mater. Trans.* **46** 2817
[39] Slater J C 1937 *J. Appl. Phys.* **8** 385
[40] Pauling L 1938 *Phys. Rev.* **54** 899
[41] Müller M, Grahl H, Mattern N, Ktihn U and Schnell B 1996 *J. Magn. Magn. Mater.* **160** 284
[42] Blázquez J S, Franco V and Conde A 2002 *J. Phys.: Condens. Matter* **14** 11717
[43] Herzer G 1989 *IEEE Trans. Magn.* **25** 3327
[44] Herzer G 2013 *Acta Mater.* **61** 718